Chemistry–A European Journal
Research Article
doi.org/10.1002/chem.202200760
Chemistry Europe
European Chemical Societies Publishing
www.chemeurj.org

Synthesis and Luminescence Properties of Amber Emitting $La_7Sr[Si_{10}N_{19}O_3]:Eu^{2+}$ and Syntheses of the Substitutional Variants $RE_{8-x}AE_x[Si_{10}N_{20-x}O_{2+x}]:Eu^{2+}$ with RE = La, Ce; AE = Ca, Sr, Ba; $0 \le x \le 2$

Lisa Gamperl,[a] Philipp Strobel,[b] Peter J. Schmidt,[b] and Wolfgang Schnick*[a]

Abstract: The oxonitridosilicate $La_7Sr[Si_{10}N_{19}O_3]:Eu^{2+}$ and its substitutional variants $RE_{8-x}AE_x[Si_{10}N_{20-x}O_{2+x}]:Eu^{2+}$ with RE = La, Ce; AE = Ca, Sr, Ba and $0 \le x \le 2$ were synthesized starting from REN, SrN/Ca_3N_2/Ba_2N, SiO_2, amorphous Si_3N_4 and Eu_2O_3 as doping agent at 1600 °C in a radiofrequency furnace. The crystal structure of $La_7Sr[Si_{10}N_{19}O_3]$ was solved and refined based on single-crystal X-ray diffraction data. $La_7Sr[Si_{10}N_{19}O_3]$ crystallizes in the orthorhombic space group $Pmn2_1$ (no. 31). The crystal structures of the isotypic compounds $RE_{8-x}AE_x[Si_{10}N_{20-x}O_{2+x}]$ were confirmed by Rietveld refinements based on powder X-ray diffraction data using the single-crystal data of $La_7Sr[Si_{10}N_{19}O_3]$ as starting point. Crystal structure elucidation reveals a 3D network of vertex sharing SiN_4 and $SiN_2(N_{1/2-x/4}O_{1/2+x/4})_2$ $(0 \le x \le 2)$ tetrahedra. When excited with UV to blue light, $La_7Sr[Si_{10}N_{19}O_3]:Eu^{2+}$ shows amber luminescence with λ_{em} = 612 nm and fwhm = 84 nm/2194 cm^{-1}, which makes it interesting for application in amber phosphor-converted light emitting diodes.

Introduction

The U.S. Department of Energy, Office of Energy Efficiency and Renewable Energy states in its latest "Energy Savings Forecast of Solid-State Lighting in General Illumination Applications" report that in 2017, 38% of the total energy consumption in the United States (U.S.) was needed for electricity use, of which lighting consumed 6% of total energy and 16% of total electricity used.[1] Thereby, solid-state lighting based on phosphor converted light emitting diodes (pcLEDs), which had their breakthrough with the invention of efficient blue light-emitting diodes based on (In,Ga)N primary LEDs by Akasaki, Amano and Nakamura, lead the revolution of the lighting market.[1,2] LEDs exceed traditional lighting technologies like incandescent light bulbs and fluorescent tubes with regard to the combination of energy efficiency, lifetime, versatility, color quality and cost efficiency and can therefore be used in a wide range of lighting applications.

Current state-of-the-art white light emitting LEDs are based on a two phosphor approach (2pcLED), for which orange-red and yellow-green emitting phosphors are used to down-convert the blue emission of the primary LED, which then results in warm white light by additive color mixing.[3,4] $(Ca,Sr)Si_2O_2N_2:Eu^{2+}$ can be used as the yellow-green emitting component, while $(Sr,Ba)_2Si_5N_8:Eu^{2+}$ or $(Sr,Ca)AlSiN_3:Eu^{2+}$ serve as orange-red emitting phosphors.[4–9] Despite the favorable properties of $(Sr,Ba)_2Si_5N_8:Eu^{2+}$ or $(Sr,Ca)AlSiN_3:Eu^{2+}$, like tunability, good thermal behavior, high efficacy and high color rendition, they suffer from energy loss by emission in the infrared spectral range (IR spillover) due to their rather broad emission bands (2050–2600 cm^{-1}).[3,10] Therefore, research is focused on exploring new highly efficient narrow-band orange-red phosphors. Promising candidates have been found with $Sr[LiAl_3N_4]:Eu^{2+}$ (SLA, λ_{em} = 650 nm, full width at half-maximum (fwhm) = 1180 cm^{-1}), $Sr[Li_2Al_2O_2N_2]:Eu^{2+}$ (SALON, λ_{em} = 614 nm, 1286 cm^{-1}) and $Sr[Mg_3SiN_4]:Eu^{2+}$ (SMS) with SMS being the so far most narrow orange-red emitting Eu^{2+} doped nitride phosphor (λ_{em} = 615 nm, fwhm = 1170 cm^{-1}).[11–13]

(Oxo)nitridosilicates are a promising compound class in the research for novel host lattices used as phosphor materials. They offer a huge structural variability as nitrogen can crosslink up to four tetrahedra centers and SiN_4 tetrahedra can be linked by sharing edges or corners. This versatility leads to high potential for applications not only in the lighting sector.[14,15] Therefore, scientific research is still focused on discovering new auspicious (oxo)nitridosilicate phosphors to further broaden the application of pcLEDs. To the best of our knowledge, only two phosphors are known so far in the La–Sr–Si–O–N system, namely $La_{26-x}Sr_xSi_{41}O_{x+1}N_{80-x}:Eu^{2+}$ (x = 12.72–12.90), which emits in the red spectral region (λ_{em} = 643 nm, fwhm = 142 nm), and narrow-band red emitting $La_{4-x}Sr_{2+x}Si_5N_{12-x}O_x:Pr^{3+}$ ($x \approx 1.69$) with

[a] L. Gamperl, Prof. Dr. W. Schnick
Department of Chemistry
University of Munich (LMU)
Butenandtstr. 5–13, 81377 Munich (Germany)
E-mail: wolfgang.schnick@uni-muenchen.de
[b] Dr. P. Strobel, Dr. P. J. Schmidt
Lumileds Germany GmbH
Lumileds Phosphor Center Aachen
Philipsstr. 8, 52068 Aachen (Germany)

Supporting information for this article is available on the WWW under https://doi.org/10.1002/chem.202200760

λ_{em} = 625 nm and fwhm = 40 nm.[16,17] Thus, the barely investigated La–Sr–Si–N–O system is promising for containing more host compounds that result in red emitting phosphors with potential for usage in lighting applications. In this contribution, we report on the synthesis and characterization of the oxonitridosilicate $La_7Sr[Si_{10}N_{19}O_3]$ and its substitutional variants $RE_{8-x}AE_x[Si_{10}N_{20-x}O_{2+x}]$ with RE = La, Ce; AE = Ca, Sr, Ba and $0 \leq x \leq 2$. Amber emitting $La_7Sr[Si_{10}N_{19}O_3]:Eu^{2+}$ exhibits an emission maximum at λ_{em} = 612 nm with a full width at half-maximum of 84 nm/2194 cm^{-1} upon excitation with UV to blue light. The observed luminescence properties will be discussed in detail.

Results and Discussion

Synthesis and chemical analysis

$La_7Sr[Si_{10}N_{19}O_3]:Eu^{2+}$ and the solid solution series of its substitutional variants $RE_{8-x}AE_x[Si_{10}N_{20-x}O_{2+x}]:Eu^{2+}$ with RE = La, Ce; AE = Ca, Sr, Ba and $0 \leq x \leq 2$ were obtained as described in the Experimental Section according to the following reaction equations using Eu_2O_3 as a dopant:

$$(8\text{-}x)\ RE\mathrm{N} + x\ \mathrm{SrN} + (2+x)/2\ \mathrm{SiO_2} + (18\text{-}x)/6\ \mathrm{Si_3N_4} \rightarrow RE_{8-x}\mathrm{Sr}_x[\mathrm{Si_{10}N_{20-x}O_{2+x}}] + x/6\ \mathrm{N_2} \quad (1)$$

$$(8\text{-}x)\ RE\mathrm{N} + x/3\ \mathrm{Ca_3N_2} + (2+x)/2\ \mathrm{SiO_2} + (18\text{-}x)/6\ \mathrm{Si_3N_4} \rightarrow RE_{8-x}\mathrm{Ca}_x[\mathrm{Si_{10}N_{20-x}O_{2+x}}] \quad (2)$$

$$(8\text{-}x)\ RE\mathrm{N} + x/2\ \mathrm{Ba_2N} + (2+x)/2\ \mathrm{SiO_2} + (18\text{-}x)/6\ \mathrm{Si_3N_4} + x/12\ \mathrm{N_2} \rightarrow RE_{8-x}\mathrm{Ba}_x[\mathrm{Si_{10}N_{20-x}O_{2+x}}] \quad (3)$$

However, for the syntheses with AE = Sr, a sevenfold excess of SrN, which can be described more precisely as $(Sr^{2+})_4[N^{3-}]_2[N_2^{2-}]$, was necessary due to decomposition of SrN at high temperatures and deposition on the cold reactor wall.[18] The synthesis of $La_7Sr[Si_{10}N_{19}O_3]:Eu^{2+}$ yielded single crystals (Figure S1) used for X-ray diffraction measurements to obtain the crystal structure. The single-crystal data were used for a Rietveld refinement based on powder X-ray diffraction data for determination of the bulk phase composition, which revealed a phase pure synthesis (Figure 1, Table S1).

The crystal structure of $La_7Sr[Si_{10}N_{19}O_3]:Eu^{2+}$ exhibits mixed occupied heavy cation sites. Therefore, the terminal representatives of the solid solution series $La_{8-x}Sr_x[Si_{10}N_{20-x}O_{2+x}]:Eu^{2+}$ with x = 0 and 2, namely $La_8[Si_{10}N_{20}O_2]:Eu^{2+}$ and $La_6Sr_2[Si_{10}N_{18}O_4]:Eu^{2+}$, were synthesized as well and the phase compositions of the obtained powders were determined by Rietveld refinements based on powder X-ray diffraction data using the single-crystal data of $La_7Sr[Si_{10}N_{19}O_3]$ as a starting point (Figure S2 and Table S2).

Furthermore, due to similar sizes and charges of both the alkaline earth ions Sr^{2+} (r(coordination number CN: 9) = 1.31 Å), Ca^{2+} (r(CN: 8/9) = 1.12/1.18 Å) and Ba^{2+} (r(CN: 9) = 1.47 Å) as well as the rare earth ions La^{3+} (r(CN: 8/9) = 1.16/1.22 Å) and Ce^{3+} (r(CN: 8/9) = 1.14/1.20 Å),[19] the solid solution series $RE_{8-x}AE_x[Si_{10}N_{20-x}O_{2+x}]:Eu^{2+}$ with RE = La, Ce; AE = Ca, Sr, Ba and $0 \leq x \leq 2$ were also synthesized and Rietveld refined based on the powder X-ray diffraction data using the obtained structure model of $La_7Sr[Si_{10}N_{19}O_3]$ as a starting point, whereby only lattice parameters and fractional coordinates of the heavy cation sites were refined. Due to similar ionic radii of Ca^{2+} and La^{3+}, it is possible that Ca occupies those sites, which in the Sr containing compound are solely occupied by La. However, it is not possible to determine which sites exactly are occupied by Ca and to which extent by the Rietveld method. Therefore, the Rietveld refinements of the Ca containing compounds were based on the obtained structure model of $La_7Sr[Si_{10}N_{19}O_3]$ without further changes. All Rietveld refinements and corresponding data are shown in Figures S2, S3 and Tables S2–S4, respectively.[19] For SEM-EDX measurements (Table S5), only the cation values and the atomic ratios (RE + AE)/Si were considered since the anion values were more affected by shadowing caused by unfavorable orientation of the crystals with respect to the EDX detector and by superficially bound oxygen on the samples. Both the measured values for the individual atoms and the calculated atomic ratios agree well within the typical limits of accuracy with the theoretical values. Although Eu could not be detected by EDX because of its small amount, its occurrence is proven by the observed luminescence. Therefore, Eu was subsequently neglected in structure refinements.

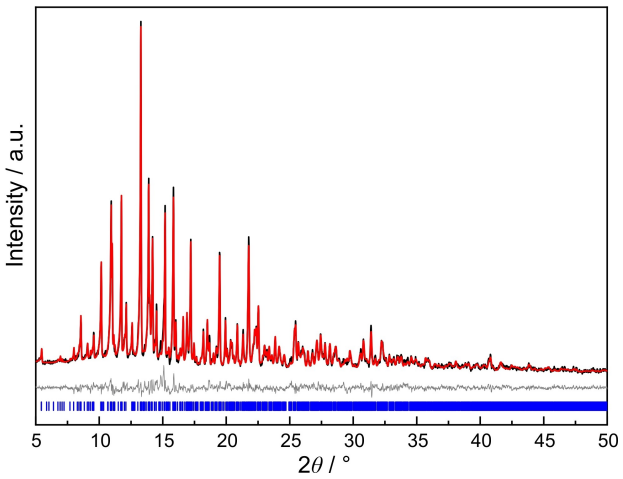

Figure 1. Rietveld refinement based on PXRD data collected from a powder sample containing $La_7Sr[Si_{10}N_{19}O_3]$ based on the structure model obtained by SCXRD data with observed (black) and calculated (red) powder X-ray diffraction patterns and the corresponding difference profile (gray). Vertical blue bars indicate the position of the Bragg reflections of the title compound.

Crystal structure elucidation

The crystal structure of $La_7Sr[Si_{10}N_{19}O_3]$ was solved and refined based on single-crystal X-ray diffraction data in the orthorhombic space group $Pmn2_1$ (no. 31). Crystallographic data is given in Table 1, while Wyckoff positions, atomic coordinates, and isotropic displacement parameters as well as anisotropic

Table 1. Crystallographic data of the single-crystal structure determination of $La_7Sr[Si_{10}N_{19}O_3]$.

sum formula	$La_7Sr[Si_{10}N_{19}O_3]$
formula weight [g mol^{-1}]	1655.08
crystal system	orthorhombic
space group	$Pmn2_1$ (no. 31)
lattice parameters [Å]	$a = 9.5027(11)$
	$b = 19.0471(19)$
	$c = 12.0753(14)$
V [Å^3]	2185.62(4)
Z	4
X-ray density [g cm^{-3}]	5.02954
abs. coefficient [μ mm^{-1}]	16.393
absorption correction	multiscan[20]
diffractometer	Bruker D8 Venture
Radiation	Mo-$K\alpha_1$ ($\lambda = 0.70930$ Å)
$F(000)$	2936
θ range [°]	$2.138 \leq \theta \leq 24.996$
independent reflections (all/with $I > 2\sigma(I)$)	4104/3910
refined parameters/restraints	220/6
R_{int}	0.0481
R_σ	0.0529
$R1$ (all data/for $I > 2\sigma(I)$)	0.0318/0.0294
$wR2$ (all data/for $I > 2\sigma(I)$)	0.0746/0.0735
$\Delta\rho_{max}/\Delta\rho_{min}$ [e Å^{-3}]	2.44/−2.39
$GooF$ (χ^2)	1.115

displacement parameters are listed in Table S6 and S7, respectively.

The structure exhibits twelve cation sites, of which eight are fully occupied with La, while four sites show a mixed occupation of La and Sr, resulting in the reported atomic ratio La:Sr of 7:1. Fully occupied sites show similar coordination spheres, distances, and polyhedron volumes among themselves, the same applies to the mixed occupied sites (Table S8). The results were supported by charge distribution (CHARDI) and bond-valence sum (BVS) calculations (Table S9).[21–25] During the refinement, an elongated anisotropic displacement parameter for Sr/La12 was observed. Therefore, a difference Fourier synthesis (F_{obs}-F_{calc}) of the electron density located at this site was calculated, however, there was no indication for splitting of the electron density at high isosurface levels (Figure S4). The elongated anisotropic displacement parameter may be explained by mixed occupation and a slightly enlarged Sr/La12-N distance (Table S8). For charge compensation, incorporation of oxygen was assumed. Eight terminal anionic sites with shorter Si-$X^{[1]}$ (X = N, O) distances are suitable for an occupation with oxygen while all other twofold bridging sites were fully occupied with nitrogen, which is in agreement with Pauling's second rule.[26] The differentiation between O and N was not only based on connectivity and distances, but also on the HSAB principle, according to which the harder Lewis acid La^{3+} is expected to be coordinated by the harder Lewis base O^{2-}.[27–29] To obtain a charge neutral composition, the eight terminal anionic sites were equally mixed occupied and constrained to 0.75 O and 0.25 N on each site, respectively. Chemically identical Si, N and N/O positions, respectively, were refined with constrained anisotropic displacement parameters.

As mixed cation and anion sites are present and LaN vs. SrO can be exchanged for each other without violating charge neutrality, solid solutions $La_{8-x}Sr_x[Si_{10}N_{20-x}O_{2+x}]$ with $0 \leq x \leq 2$ resulting in $La_8[Si_{10}N_{20}O_2]$ with fully La occupied cation sites and each terminal anionic site occupied with 0.5 O and 0.5 N, respectively, and $La_6Sr_2[Si_{10}N_{18}O_4]$ with the previously mixed occupied sites now fully occupied by Sr and O, respectively, were obtained. Due to similar ionic radii, solid solution series of the substitutional variants with La exchanged by Ce and Sr exchanged by Ca and Ba were synthesized, resulting in an overall sum formula $RE_{8-x}AE_x[Si_{10}N_{20-x}O_{2+x}]$ (RE = La, Ce; AE = Ca, Sr, Ba; $0 \leq x \leq 2$).

Structure description

$La_7Sr[Si_{10}N_{19}O_3]$ exhibits a three-dimensional network (Figure 2) of vertex sharing Q^4-type $SiN^{[2]}_4$ and Q^2-type $SiN^{[2]}_2(N_{0.25}O_{0.75})^{[1]}_2$ tetrahedra.[30,31]

The structure can be divided into two quasi-identical, but slightly tilted ribbons along [001] consisting of SiN_4 tetrahedra, one ribbon colored in blue shades, the other one in green shades, respectively (Figure 3, S5).

The ribbons can be subdivided into two units depicted in dark and light shades, where both the dark blue and green units and the light blue and green units, respectively, are quasi-identical among each other but slightly tilted (Figure 4).

The darker units form a cage consisting of three *sechser* rings, while the lighter units can be described as an inverted structure formally formed by a mirror plane at $a/2$ crossing at half of the cage (Figure S5).[32] The units are interconnected via common vertices, whereby a cage is surrounded by four inverted structures and vice versa leading to additional cages. Q^2-type $SiN^{[2]}_2(N_{0.25}O_{0.75})^{[1]}_2$ tetrahedra are only interconnect within one unit or equal units along [100] forming *dreier* rings in the (100) plane (Figure S5). Accordingly, the seeming *achter* ring channels as viewed along [100] are not closed *achter* rings

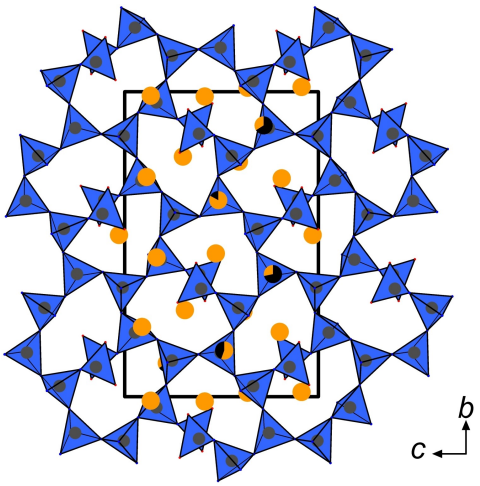

Figure 2. Crystal structure of $La_7Sr[Si_{10}N_{19}O_3]$. $Si(N,O)_4$ tetrahedra in blue, Si atoms dark gray, La atoms orange, Sr atoms black. Mixed occupied cation sites colored in the respective atom colors with the section size corresponding to the percentage occupancy.

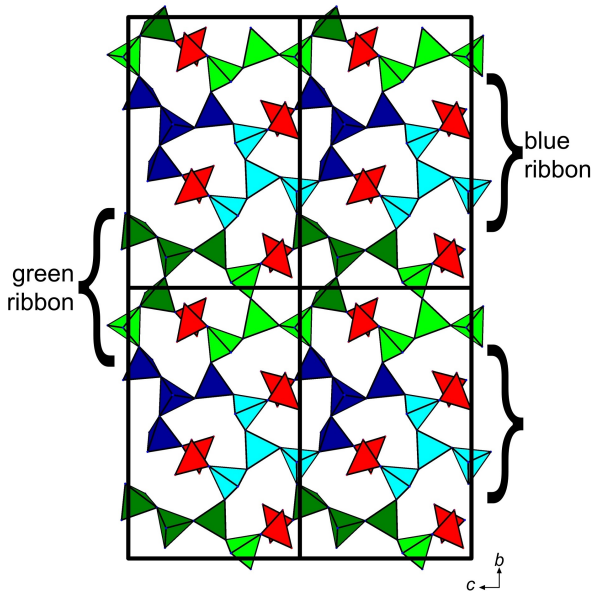

Figure 3. 2×2×2 super cell viewed along [100] of $La_7Sr[Si_{10}N_{19}O_3]$ illustrating the substructure consisting of two different ribbons. SiN_4 tetrahedra in blue and green shades, $SiN_2(N_{0.25}O_{0.75})_2$ in red.

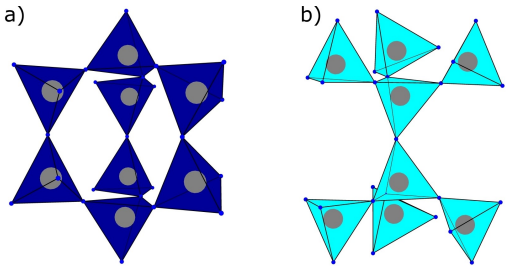

Figure 4. Eight SiN_4 tetrahedra forming a) a cage or b) an inverted structure. Si atoms dark gray, N atoms blue.

but intersecting counterclockwise and clockwise distorted screws along [100] with internal offsets of 5.59(2) and 5.62(2) Å, respectively (Figure S6).

La and Sr occupy twelve cation sites, of which eight are solely occupied by La (Figure S7). These sites are coordinated by six N and two N/O in form of partly more or less distorted hexagonal bipyramids, respectively. Four sites are mixed occupied by La and Sr and coordinated solely by nine N in form of distorted triple capped trigonal prisms. These sites are located inside the cavities formed by the cages.

Interatomic La–N/O distances are in the range of 2.41(2)–3.30(2) Å, while Sr/La–N distances vary from 2.62(2) to 3.37(2) Å and Si–N/O distances are between 1.65(1) to 1.77(1) Å and Si–N between 1.64(2) to 1.70(2) Å, which are in good agreement with reported values of other *RE*–*AE*–Si–N–O compounds.[33–41] For the substitutional variants $RE_{8-x}AE_x[Si_{10}N_{20-x}O_{2+x}]:Eu^{2+}$ (*RE* = La, Ce; *AE* = Ca, Sr, Ba; $0 \le x \le 2$), the mixed occupied sites La/Sr9-12 can be substituted by Ce and Ca or Ba, respectively, whereas Ca^{2+} could also occupy solely La^{3+} occupied sites due to similar ionic radii. For charge compensation, this requires the simultaneous incorporation of oxygen on the mixed occupied anionic sites, leading to $SiN_2(N_{1/2-x/4}O_{1/2+x/4})_2$ ($0 \le x \le 2$) tetrahedra.

UV/Vis reflectance spectroscopy

For the determination of the optical band gap of nondoped $La_7Sr[Si_{10}N_{19}O_3]$, UV/Vis spectroscopy was used. The measured diffuse reflectance spectrum was transformed into a pseudo-absorption spectrum applying the Kubelka-Munk function $F(R) = (1-R)^2/2R$ (R = measured reflectance).[42] The optical band gap was determined from a Tauc plot, whereby $h\nu$ is plotted against $(F(R)\cdot h\nu)^{1/n}$ with $n = 1/2$ for a direct allowed transition by intersecting the aligned tangent on the linear region with the abscissa.[43] Thereby, the optical band gap was estimated to be approximately 3.55 eV (Figure 5), although host materials with larger band gaps $\geq$4 eV are desired for pcLED applications.[13,17,44–48]

Luminescence

Luminescence properties were measured on single luminescent particles of Eu^{2+} doped $La_7Sr[Si_{10}N_{19}O_3]$. Upon excitation of the samples with UV to blue light, $La_7Sr[Si_{10}N_{19}O_3]:Eu^{2+}$ (0.2 mol%) shows orange luminescence and exhibits an emission maximum at $\lambda_{em} = 612$ nm with fwhm = 84 nm/2194 cm^{-1} (Figure 6). Due to the excitation maximum at $\lambda_{exc} \approx 445$ nm, $La_7Sr[Si_{10}N_{19}O_3]:Eu^{2+}$ (0.2 mol%) can efficiently be excited by an (In,Ga)N LED light source.

The rather broad emission band can be assigned to the parity-allowed $4f^65d^1$ (^7F) $\rightarrow 4f^7$ ($^8S_{7/2}$) transition of Eu^{2+}.[49]

The emission properties of $La_7Sr[Si_{10}N_{19}O_3]:Eu^{2+}$ (0.2 mol%) can be compared to other amber emitting phosphors that already found applications like $(Ba,Sr)_2Si_5N_8:Eu^{2+}$ ($\lambda_{em} \approx 590$–625 nm, fwhm ≈2050–2600 cm^{-1}) and $(Sr,Ca)AlSiN_3:Eu^{2+}$ (λ_{em} ≈610–660 nm, fwhm ≈2100–2500 cm^{-1}) or other oxonitridosilicates like $Y_4Ba_2[Si_9ON_{16}]O:Eu^{2+}$ ($\lambda_{em} = 622$ nm, fwhm = 111 nm/

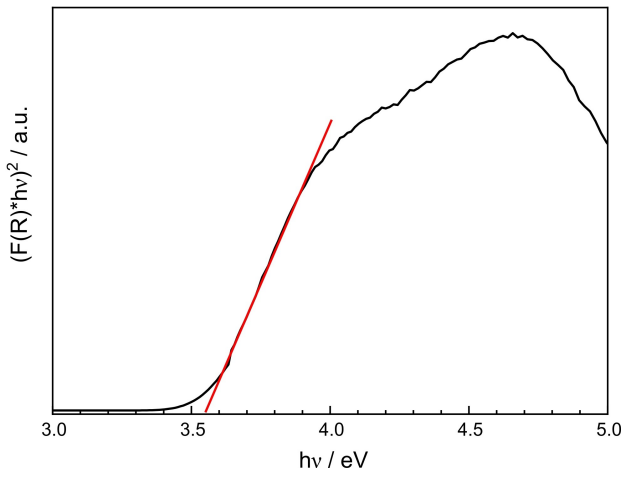

Figure 5. Tauc plot ($n = 1/2$) for a nondoped $La_7Sr[Si_{10}N_{19}O_3]$ powder sample. The artifact around 3.65 eV (340 nm) corresponds to the lamp switch.

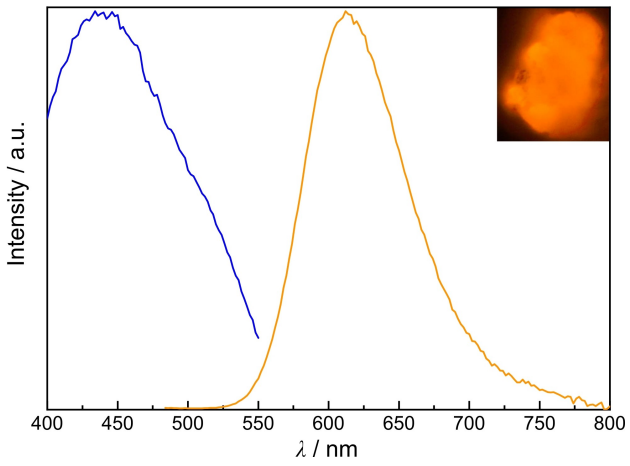

Figure 6. Normalized excitation (blue, $\lambda_{mon} = 608$ nm) and emission spectra (orange, $\lambda_{exc} = 450$ nm) of $La_7Sr[Si_{10}N_{19}O_3]:Eu^{2+}$ (0.2 mol%) with a micrograph of the measured particle.

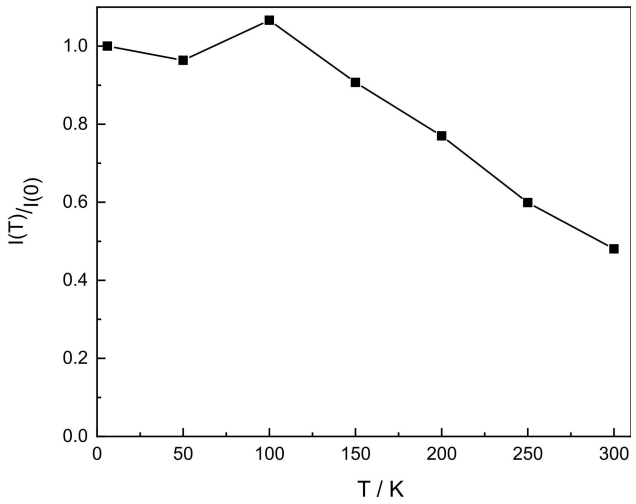

Figure 7. Temperature dependent relative integrated emission intensities of $La_7Sr[Si_{10}N_{19}O_3]:Eu^{2+}$ (0.2 mol%).

2875 cm^{-1}).[4–9,47] Phosphors of other compound classes like $Sr[Mg_3SiN_4]$ ($\lambda_{em} = 615$ nm, fwhm = 43 nm/1170 cm^{-1}), $Sr[Li_2Al_2O_2N_2]$ ($\lambda_{em} = 614$ nm, fwhm = 48 nm/1286 cm^{-1}) or $Sr[Mg_2Al_2N_4]$ ($\lambda_{em} = 612$ nm, fwhm = 1823 cm^{-1}) show similar emission maxima but more narrow emission bands due to higher symmetric crystal structures and fewer but higher symmetric activator sites.[12,13,50]

Samples of $La_7Sr[Si_{10}N_{19}O_3]:Eu^{2+}$ exhibit little intense luminescence presumably due to the small band gap that may give rise to thermal de-excitation via the conduction band. Merely, a low doping concentration of 0.2 mol% lead to measurable luminescence making quantum efficiency determinations of doping series unreliable (IQE $\ll$10%), although room temperature luminescence was visible for samples with different doping levels and variation of *RE* and *AE*. Solely, a bulk sample of $Ce_6Ca_2[Si_{10}N_{18}O_4]:Eu^{2+}$ was measurable, resulting in $\lambda_{em} =$ 627 nm with fwhm = 139 nm/3516 cm^{-1} (Figure S10), whereby the red shift of the luminescence maximum compared to $La_7Sr[Si_{10}N_{19}O_3]:Eu^{2+}$ is in agreement with the decreasing cation sizes causing an increased Stokes shift.

Due to the weak luminescence at room temperature, cryospectroscopy measurements were recorded to determine whether the luminescence intensity increases at lower temperatures (Figure 7).

As it can be derived from Figure 7, the luminescence intensity at 6 K was merely higher by a factor of about 2.

There are two predominant theories to describe the thermal quenching behavior of activator ions in phosphors: the crossover mechanism according to Blasse et al. and the thermal ionization mechanism after Dorenbos (Figure S8).

The crossover mechanism results from nonradiative relaxation of the excited activator $5d^1$ electron to the ground state when the temperature is sufficiently high to exceed an activation energy. This activation energy is defined as the energy difference between the vibrationally relaxed but electronically excited state and the intersection of the parabola axes of the ground and excited states, which can be illustrated in a configurational coordinate diagram (Figure S8). Therefore, research is focused on structurally rigid host materials because rigid structures allow only few vibrational modes, reducing the probability of nonradiative relaxation. Rigidity can be indicated by the degree of condensation κ, defined as the ratio of tetrahedra centers to its coordinating anions, and the number of multi-bridging atoms like N[3] or N.[4] However, stability against local shifts within an activator vicinity are more reliable compared to a general descriptor such as structural rigidity.[44,49,51] Thermal quenching induced by the thermal ionization mechanism can be described by thermally overcoming the activation energy for elevation of the excited activator $5d^1$ electron to the conduction band minimum of the host. Resonant inelastic X-ray scattering (RIXS) measurements have been used to determine the influence of the host lattice on the highly sensitive position of the 5*d* levels of the activator ion and therefore, the 5*d* to conduction band separation. The position of the 5*d* levels is influenced by effects caused by the ligand field surrounding the activator ions namely, among other things, by the nephelauxetic effect, centroid shift, and crystal field splitting, which depend on the host material. The valence band maximum is mainly dominated by N and O *p*-states while the conduction band minimum is formed by network forming elements like Si or by elements filling up the network structures such as *RE* or *AE*. Going from Ca to Ba *d*-states, the band gap decreases due to the lower energy of Ba *d*-states.[17,44,45,52,53] The determination of the 5*d* to conduction band separation by RIXS can be a very useful tool for the distinction whether thermal quenching is an intrinsic material property when the separation is determined to be small or if thermal quenching is extrinsically influenced and can be reduced by optimizing the synthesis.[44,45,52] The influence of thermal ionization and crossover mechanisms compete and depend on the size of the band gap of the host material, whereas the influence of the crossover mechanism increases for lager band gaps ($E_g > 4$ eV). With

smaller band gaps, it is possible that both mechanisms occur simultaneously.[44]

An important factor to consider in this context is the Stokes shift, which correlates with the energetic position of the excitation and emission bands as well as with the width of those bands and negatively influences thermal quenching behavior and thus the luminescence efficiency. According to Equation (4),[51]

$$E_{\text{Stokes}} = 2S \cdot \hbar\omega \quad (4)$$

the Stokes shift depends on the phonon frequencies ω of local lattice vibrations and is related to the atomic weight of the host material atoms, with smaller ω for larger molar masses. The Huang-Rhys parameter S is a scale for the magnitude of the electron-phonon coupling and therefore depends on the rigidity of the host lattice, with low rigidity corresponding to large values of S.[51,54–57] In the case of $La_7Sr[Si_{10}N_{19}O_3]$, the degree of condensation equals $\kappa = n(\text{Si})/n(\text{N,O}) = 10/22 \approx 0.45$ and consists besides terminal mixed occupied $(N,O)^{[1]}$ sites solely of twofold bridging $N^{[2]}$ sites. Therefore, $La_7Sr[Si_{10}N_{19}O_3]$ cannot be denominated as a highly condensed network and may suffer from reduced structural rigidity. This leads to larger values for both S and E_{Stokes}, so the parabola offset (Figure S9) increases and the crossover of the two parabola axes occur at lower E. Therefore, the activation energy for the crossover mechanism decreases, leading to a higher probability for thermal quenching.

Since cryo-spectroscopy measurements did not result in stronger luminescence, thermal ionization may not be the determining factor for the observed thermal quenching despite the comparably small band gap. The rather large Stokes shift due to low structural rigidity leads to an increased probability for thermal quenching according to the crossover mechanism as the determining factor in $La_7Sr[Si_{10}N_{19}O_3]$.

Conclusion

In this contribution, we report on the syntheses of $La_7Sr[Si_{10}N_{19}O_3]:Eu^{2+}$ and the solid-solution series of its substitutional variants $RE_{8-x}AE_x[Si_{10}N_{20-x}O_{2+x}]$ with RE = La, Ce; AE = Ca, Sr, Ba and $0 \le x \le 2$. $La_7Sr[Si_{10}N_{19}O_3]:Eu^{2+}$ is only the second known Eu^{2+} doped phosphor in the La–Sr–Si–O–N system so far. The crystal structure of $La_7Sr[Si_{10}N_{19}O_3]$ was solved and refined in the orthorhombic space group $Pmn2_1$ (no. 31) based on single-crystal X-ray diffraction data. It exhibits a new three- dimensional network of vertex sharing $SiN^{[2]}_4$ and $SiN^{[2]}_2(N_{0.25}O_{0.75})^{[1]}_2$ tetrahedra leading to a cage like structure filled by sites occupied solely by lanthanum or mixed occupied by lanthanum and strontium. Due to the mixed cation and anion sites and the charge neutral exchangeability of LaN vs. SrO, the solid solution series $La_{8-x}Sr_x[Si_{10}N_{20-x}O_{2+x}]$ with $0 \le x \le 2$ was synthesized. In addition to that, similar ionic radii of La and Ce as well as Sr, Ca and Ba led to the syntheses of the solid solution series of the substitutional variants $RE_{8-x}AE_x[Si_{10}N_{20-x}O_{2+x}]$ (RE = La, Ce; AE = Ca, Sr, Ba; $0 \le x \le 2$). This was confirmed by Rietveld refinements based on powder X-ray diffraction data using the obtained structure model of $La_7Sr[Si_{10}N_{19}O_3]$ as a starting point and by EDX measurements. The compound class $RE_{8-x}AE_x[Si_{10}N_{20-x}O_{2+x}]$ offers a broad variety of full or partial substitution possibilities and therefore, could be an interesting host material class for tunability upon Eu^{2+} doping. Solid-state UV/Vis spectroscopy was used to determine the optical band gap of nondoped $La_7Sr[Si_{10}N_{19}O_3]$ and resulted in a comparable small band gap of $E_g \approx 3.55$ eV. Luminescence measurements on single particles of 0.2 mol% doped $La_7Sr[Si_{10}N_{19}O_3]:Eu^{2+}$ led to amber emission upon excitation with UV to blue light with an emission maximum at $\lambda_{em} \approx 612$ nm and fwhm ≈ 84 nm/2194 cm^{-1}. The emission characteristics are comparable to commercially utilized amber emitting $(Ba,Sr)_2Si_5N_8:Eu^{2+}$ and $(Sr,Ca)AlSiN_3:Eu^{2+}$. Since the luminescence at room temperature was weak, cryo-spectroscopy was used to investigate whether the luminescence intensity can be raised at lower temperatures which resulted in a factor of 2 higher intensity. The two predominant theories for explaining the thermal quenching behavior of activator ions in phosphors, namely the crossover mechanism according to Blasse et al. and the thermal ionization mechanisms after Dorenbos, were discussed. Due to the comparable small band gap, both quenching mechanisms probably occur simultaneously. Thermal ionization may not be the determining factor because cryo-spectroscopy measurements did not result in significantly higher luminescence. The crystal structure of $La_7Sr[Si_{10}N_{19}O_3]$ appears to offer less structural rigidity, which leads to a larger Stokes shift and therefore increases the probability for thermal quenching as described by the crossover mechanism. Further syntheses of $RE_{8-x}AE_x[Si_{10}N_{20-x}O_{2+x}]:Eu^{2+}$ and extensive investigations regarding luminescence properties, band structures and RIXS measurements are necessary to further understand the influences of different RE and AE on band structures, band gap sizes and position of Eu 5d levels. With this knowledge, potential host materials and their luminescent properties can be improved and possibly be tunable to develop the highly desired narrow-band and super-efficient red phosphors.

Experimental Section

Synthesis: Due to some air and moisture sensitive starting materials, all manipulations were carried out under argon atmosphere either in an Ar filled glovebox (Unilab, MBraun, Garching; $O_2 < 1$ ppm; $H_2O < 1$ ppm) or in Ar-filled glassware applying the Schlenk technique. For the synthesis of the starting materials SrN and CeN used as for the main syntheses, the respective metals were first placed in a tungsten crucible and then positioned into a corundum crucible. This assembly was transferred into the pressure chamber of a hot isostatic press (HIP, AIP6-30H, American Isostatic Presses, Inc., Columbus, Ohio, USA) equipped with a carbon fiber reinforced carbon furnace ($T_{max} = 2000$ °C, ø = 70 mm, $h = 125$ mm). The atmosphere in the pressure vessel ($p_{max} = 207$ MPa) was first flushed with N_2 for 10 times and then, a pressure booster (Maximator, DLE-5-30-2, $p_{max} = 60$ MPa) to build up the necessary pressure to operate the main compressor was used. When the pressure was subsequently increased and reached 70 MPa, the samples were heated to 1000 °C within 3.5 h while ending up with a pressure of 150 MPa. After heating for 10 h, the setup was cooled

down to 20 °C and the pressure was released. SrN and CeN were obtained as black and dark brown powders, respectively (see Figure S11 and Table S10). The chemicals required for the phase-pure syntheses of $RE_{8-x}AE_x[Si_{10}N_{20-x}O_{2+x}]$ (RE = La, Ce; AE = Ca, Sr, Ba; $0 \leq x \leq 2$), as well as their respective amounts are listed in Tables S11 and S12. The thoroughly ground starting materials were filled into a tungsten crucible and transferred into a water-cooled silica glass reactor of a radiofrequency furnace (TIG 10/100; Hüttinger Elektronik Freiburg, Germany) attached to a Schlenk line.[58] The crucible was heated within 5 min to 1600 °C under N_2 atmosphere, maintained at that temperature for 5 h, cooled down to 1200 °C within 15 h, and finally quenched by switching off the furnace. All body colors and luminescence impressions are listed in Table S13.

Single-crystal X-ray diffraction: A single crystal of $La_7Sr[Si_{10}N_{19}O_3]$ was isolated and fixed on a MicroMount (50 μm, MiTeGen, Ithaca, New York, USA). X-ray diffraction data were collected with a Bruker D8 Venture diffractometer with rotating anode (Mo-Kα radiation). For indexing, integration, semi-empirical absorption correction and determination of the space group, the software package APEX3 was used, while WinGX with the implemented tools SHELXT and SHELXL was used for structure solution and refinement by full-matrix least-squares method.[20,59–65] Deposition Numbers can be found in Table S14 and contain the supplementary crystallographic data for this paper. These data are provided free of charge by the joint Cambridge Crystallographic Data Centre and Fachinformationszentrum Karlsruhe Access Structures service (http:// www.ccdc.cam.ac.uk/structures).

Deposition Number(s) 2104245 (for $La_7Sr[Si_{10}N_{19}O_3]$), 2141282 (for $La_8[Si_{10}N_{20}O_2]$), 2141280 (for $La_6Sr_2[Si_{10}N_{18}O_4]$), 2141281 (for $La_7Ca[Si_{10}N_{19}O_3]$), 2141318 (for $La_6Ca_2[Si_{10}N_{18}O_4]$), 2141284 (for $La_7Ba[Si_{10}N_{19}O_3]$), 2141283 (for $La_6Ba_2[Si_{10}N_{18}O_4]$), 2141285 (for $Ce_7Sr[Si_{10}N_{19}O_3]$), 2141287 (for $Ce_8[Si_{10}N_{20}O_2]$), 2141319 (for $Ce_6Sr_2[Si_{10}N_{18}O_4]$), 2141288 (for $Ce_7Ca[Si_{10}N_{19}O_3]$), 2141289 (for $Ce_6Ca_2[Si_{10}N_{18}O_4]$), 2141290 (for $Ce_7Ba[Si_{10}N_{19}O_3]$), 2141320 (for $Ce_6Ba_2[Si_{10}N_{18}O_4]$) contain(s) the supplementary crystallographic data for this paper. These data are provided free of charge by the joint Cambridge Crystallographic Data Centre and Fachinformationszentrum Karlsruhe Access Structures service.

Powder X-ray diffraction: For the collection of powder X-ray diffraction (PXRD) data of the ground products sealed into glass capillaries (0.2 mm diameter, wall thickness 0.01 mm; Hilgenberg GmbH, Malsfeld, Germany), a STOE STADI P diffractometer (Mo-Kα_1 radiation, $\lambda = 0.70930$ Å, Stoe & Cie, Darmstadt, Germany) equipped with an Ge(111) monochromator and a Mythen1 K detector (Dectris, Baden-Dättwil, Switzerland) in parafocusing Debye-Scherrer geometry was used. The TOPAS Academic V6 package applying the fundamental parameters approach (direct convolution of source emission profiles, axial instrument contributions, crystallite size and microstrain effects) was used to perform Rietveld refinements.[66,67] Absorption effects were corrected using the calculated absorption coefficient. A spherical harmonics model of fourth order was applied to describe preferred orientation, while the background was modeled with a shifted Chebychev function.[68–70]

Scanning electron microscopy (SEM) and energy-dispersive X-ray spectroscopy (EDX): Energy dispersive X-ray (EDX) measurements were used to investigate the chemical composition and morphology of the samples, for which a Dualbeam Helios Nanolab G3 UC (FEI, Hillsboro, Oregon, USA) equipped with an X–Max 80 SDD detector (Oxford Instruments, Abingdon, UK) was used. The samples were carbon-coated to prevent electrostatic charging of the samples using a high-vacuum sputter coater (CCU-010, Safematic GmbH, Zizers, Switzerland).

UV/Vis spectroscopy: A Jasco V-650 UV/Vis spectrophotometer equipped with a deuterium and a halogen lamp (Czerny-Turner monochromator with 1200 lines/mm concave grating, photomultiplier tube detector) was used to measure diffuse reflectance spectra in the range of 240 to 800 nm with 1 nm step size.

Luminescence: Photoluminescence properties of Eu^{2+} doped samples were measured at room temperature on a HORIBA Fluoromax4 spectrofluorimeter system connected to an Olympus BX51 microscope via optical fibers. Excitation spectra were acquired with the monitoring wavelength λ_{mon} ranging from 425 to 516 nm. For cryo-spectroscopy between 300 and 6 K measured on a thick-bed powder layer, a fiber-coupled spectroscopy system containing a thermally stabilized LED light source and a fiber-optic spectrometer (HR2000 + ES spectrometer, Ocean Optics) was used. During the measurement, the sample was placed in an evacuated cooling chamber, equipped with a liquid-He compressor system (ARS4HW, Advanced Research System Inc., Macungie, Pennsylvania, USA).

Acknowledgements

Open Access funding enabled and organized by Projekt DEAL.

Conflict of Interest

The authors declare no conflict of interest.

Data Availability Statement

The data that support the findings of this study are available in the supplementary material of this article.

Keywords: high-temperature chemistry · luminescence · nitridosilicates · rare earths · solid-state reactions

[1] C. Elliott, M. Yamada, J. Penning, S. Schober, K. Lee, *Energy Savings Forecast of Solid-State Lighting in General Illumination Applications*, U. S. Department of Energy, Office of Energy Efficiency and Renewable Energy, Building Technologies Office, Washington, D. C., **2019**.
[2] J. Heber, *Nat. Phys.* **2014**, *10*, 791.
[3] J. L. Leaño Jr., M.-H. Fang, R.-S. Liu, *ECS J. Solid State Sci. Technol.* **2018**, *7*, R3111–R3133.
[4] R. Mueller-Mach, G. Mueller, M. R. Krames, H. A. Höppe, F. Stadler, W. Schnick, T. Juestel, P. Schmidt, *Phys. Status Solidi A* **2005**, *202*, 1727–1732.
[5] M. Krames, G. O. Mueller, R. Mueller-Mach, H. Bechtel, P. J. Schmidt, *PCT Int. Appl.* **2010**, WO2010131133 A1.
[6] H. A. Höppe, H. Lutz, P. Morys, W. Schnick, A. Seilmeier, *J. Phys. Chem. Solids* **2000**, *61*, 2001–2006.
[7] H. Watanabe, N. Kijima, *J. Alloys Compd.* **2009**, *475*, 434–439.
[8] K. Uheda, N. Hirosaki, Y. Yamamoto, A. Naito, T. Nakajima, H. Yamamoto, *Electrochem. Solid-State Lett.* **2006**, *9*, H22–H25.
[9] K. Uheda, N. Hirosaki, H. Yamamoto, *Phys. Status Solidi A* **2006**, *203*, 2712–2717.
[10] P. Pust, P. J. Schmidt, W. Schnick, *Nat. Mater.* **2015**, *14*, 454–458.
[11] P. Pust, V. Weiler, C. Hecht, A. Tücks, A. S. Wochnik, A.-K. Henß, D. Wiechert, C. Scheu, P. J. Schmidt, W. Schnick, *Nat. Mater.* **2014**, *13*, 891–896.
[12] G. J. Hoerder, M. Seibald, D. Baumann, T. Schröder, S. Peschke, P. C. Schmid, T. Tyborski, P. Pust, I. Stoll, M. Bergler, C. Patzig, S. Reißaus, M.

Krause, L. Berthold, T. Höche, D. Johrendt, H. Huppertz, *Nat. Commun.* **2019**, *10*, 1824–1832.
[13] S. Schmiechen, H. Schneider, P. Wagatha, C. Hecht, P. J. Schmidt, W. Schnick, *Chem. Mater.* **2014**, *26*, 2712–2719.
[14] W. Schnick, H. Huppertz, *Chem. Eur. J.* **1997**, *3*, 679–683.
[15] M. Zeuner, S. Pagano, W. Schnick, *Angew. Chem. Int. Ed.* **2011**, *50*, 7754–7775; *Angew. Chem.* **2011**, *123*, 7898–7920.
[16] Y. Zhang, S. Li, T. Takeda, S. Funahashi, N. Hirosaki, R.-J. Xie, *J. Mater. Chem. C* **2020**, *8*, 13458–13466.
[17] H.-W. Zheng, X.-M. Wang, H.-W. Wei, Y. Zheng, C.-L. Yin, Z.-P. Yang, H. Jiao, *Chem. Commun.* **2021**, *57*, 3761–3764.
[18] G. Auffermann, Y. Prots, R. Kniep, *Angew. Chem. Int. Ed.* **2001**, *40*, 547–549; *Angew. Chem.* **2001**, *113*, 565–567.
[19] R. D. Shannon, *Acta Crystallogr. Sect. A* **1976**, *32*, 751–767.
[20] G. M. Sheldrick, *SADABS Version 2: Multi-Scan Absorption Correction*, Bruker AXS Inc., Madison, Wisconsin, USA, **2012**.
[21] K. Momma, F. Izumi, *J. Appl. Crystallogr.* **2011**, *44*, 1272–1276.
[22] R. Hoppe, S. Voigt, H. Glaum, J. Kissel, H. P. Müller, K. Bernet, *J. Less-Common Met.* **1989**, *156*, 105–122.
[23] A. S. Wills, *VaList, v. 4.0.7*, University College London, UK, **2010**.
[24] I. D. Brown, D. Altermatt, *Acta Crystallogr. Sect. B* **1985**, *41*, 244–247.
[25] N. E. Brese, M. O'Keeffe, *Acta Crystallogr. Sect. B* **1991**, *47*, 192–197.
[26] P. E. D. Morgan, *J. Mater. Sci.* **1986**, *21*, 4305–4309.
[27] R. G. Pearson, *J. Chem. Educ.* **1968**, *45*, 581–587.
[28] R. G. Pearson, *J. Chem. Educ.* **1968**, *45*, 643–648.
[29] R. G. Pearson, *Inorg. Chim. Acta* **1995**, *240*, 93–98.
[30] Superscript numbers in square brackets within a sum formula indicate the coordination number according to the Niggli notation. U. Müller, *Anorganische Strukturchemie, Vol. 6*, Vieweg + Teubner, Wiesbaden, **2009**.
[31] J. Lima-de-Faria, E. Hellner, F. Liebau, E. Makovicky, E. Parthé, *Acta Crystallogr. Sect. A* **1990**, *46*, 1–11.
[32] The term *sechser* (*dreier*, *achter*) ring was established by F. Liebau and is derived from the German word "sechser" ("dreier", "achter"). A *sechser* (*dreier*, *achter*) ring comprises six (three, eight) tetrahedra centers. F. Liebau, *Structural Chemistry of Silicates*, Springer, Berlin, **1985**.
[33] D. Durach, P. Schultz, O. Oeckler, W. Schnick, *Inorg. Chem.* **2016**, *55*, 3624–3629.
[34] Z. A. Gál, P. M. Mallinson, H. J. Orchard, S. J. Clarke, *Inorg. Chem.* **2004**, *43*, 3998–4006.
[35] H. Ma, X. Li, R. Ye, Y. Hua, *J. Alloys Compd.* **2017**, *703*, 486–499.
[36] O. Oeckler, F. Stadler, T. Rosenthal, W. Schnick, *Solid State Sci.* **2007**, *9*, 205–212.
[37] T. Schlieper, W. Milius, W. Schnick, *Z. Anorg. Allg. Chem.* **1995**, *621*, 1380–1384.
[38] C. Schmolke, S. Lupart, W. Schnick, *Solid State Sci.* **2009**, *11*, 305–309.
[39] J. Takahashi, H. Yamane, N. Hirosaki, Y. Yamamoto, T. Suehiro, T. Kamiyama, M. Shimada, *Chem. Mater.* **2003**, *15*, 1099–1104.
[40] Z. Xia, M. S. Molokeev, W. B. Im, S. Unithrattil, Q. Liu, *J. Phys. Chem. C* **2015**, *119*, 9488–9495.
[41] H. Yamane, T. Nagura, T. Miyazaki, *Acta Crystallogr. Sect. E* **2014**, *70*, i23–i24.
[42] R. López, R. Gómez, *J. Sol-Gel Sci. Technol.* **2012**, *61*, 1–7.
[43] J. Tauc, R. Grigorovici, A. Vancu, *Phys. Status Solidi B* **1966**, *15*, 627–637.
[44] M. Amachraa, Z. Wang, C. Chen, S. Hariyani, H. Tang, J. Brgoch, S. P. Ong, *Chem. Mater.* **2020**, *32*, 6256–6265.
[45] T. M. Tolhurst, P. Strobel, P. J. Schmidt, W. Schnick, A. Moewes, *Chem. Mater.* **2017**, *29*, 7976–7983.
[46] T. M. Tolhurst, S. Schmiechen, P. Pust, P. J. Schmidt, W. Schnick, A. Moewes, *Adv. Opt. Mater.* **2016**, *4*, 584–591.
[47] C. Maak, R. Niklaus, F. Friedrich, A. Mähringer, P. J. Schmidt, W. Schnick, *Chem. Mater.* **2017**, *29*, 8377–8384.
[48] C. Maak, D. Durach, C. Martiny, P. J. Schmidt, W. Schnick, *Chem. Mater.* **2018**, *30*, 3552–3558.
[49] G. Blasse, B. C. Grabmaier, *Luminescent Materials*, Springer, Berlin, Heidelberg, **1994**.
[50] P. Pust, F. Hintze, C. Hecht, V. Weiler, A. Locher, D. Zitnanska, S. Harm, D. Wiechert, P. J. Schmidt, W. Schnick, *Chem. Mater.* **2014**, *26*, 6113–6119.
[51] G. Blasse, A. Bril, *Philips Tech. Rev.* **1970**, *31*, 304–332.
[52] P. Dorenbos, *J. Phys. Condens. Matter* **2005**, *17*, 8103–8111.
[53] T. M. Tolhurst, C. Braun, W. Schnick, A. Moewes, *J. Phys. Chem. C* **2021**, *125*, 25799–25806.
[54] G. G. Stokes, *Philos. Trans. R. Soc. London* **1852**, *142*, 463–562.
[55] G. Blasse, *Prog. Solid State Chem.* **1988**, *18*, 79–171.
[56] S. Shionoya, W. M. Yen, *Phosphor Handbook*, CRC Press, New York, **1998**.
[57] M. de Jong, L. Seijo, A. Meijerink, F. T. Rabouw, *Phys. Chem. Chem. Phys.* **2015**, *17*, 16959–16969.
[58] W. Schnick, H. Huppertz, R. Lauterbach, *J. Mater. Chem.* **1999**, *9*, 289–296.
[59] Data Integration Software, *SAINT*, Madison, Wisconsin, USA, **1997**.
[60] Bruker AXS Inc., *APEX3*, Karslruhe, Germany, **2016**.
[61] Bruker AXS Inc., *XPREP Reciprocal Space Exploration*, Karlsruhe, Germany, **2001**.
[62] L. J. Farrugia, *J. Appl. Crystallogr.* **2012**, *45*, 849–854.
[63] G. M. Sheldrick, *Acta Crystallogr. Sect. A* **2008**, *64*, 112–122.
[64] G. M. Sheldrick, *Acta Crystallogr. Sect. A* **2015**, *71*, 3–8.
[65] G. M. Sheldrick, *Acta Crystallogr. Sect. C* **2015**, *71*, 3–8.
[66] A. A. Coelho, *TOPAS Version 6: A program for Rietveld refinement*, Coelho Software, Brisbane, Australia, **2016**.
[67] H. Rietveld, *J. Appl. Crystallogr.* **1969**, *2*, 65–71.
[68] J. Bergmann, R. Kleeberg, A. Haase, B. Breidenstein, *Mater. Sci. Forum* **2000**, *347–349*, 303–308.
[69] R. W. Cheary, A. A. Coelho, J. P. Cline, *J. Res. Natl. Inst. Stand. Technol.* **2004**, *109*, 1–25.
[70] R. W. Cheary, A. Coelho, *J. Appl. Crystallogr.* **1992**, *25*, 109–121.

Manuscript received: March 9, 2022
Accepted manuscript online: April 21, 2022